SCIENCE CHINA
Physics, Mechanics & Astronomy

• Article •

January 2019 Vol. 62 No. 1: 011012
https://doi.org/10.1007/s11433-018-9272-4

Explore the QCD phase transition phenomena from a multiphase transport model

XiaoHai Jin[1,2], JinHui Chen[1*], ZiWei Lin[3,4], GuoLiang Ma[1], YuGang Ma[1*], and Song Zhang[1]

[1] *Shanghai Institute of Applied Physics, Chinese Academy of Sciences, Shanghai 201800, China;*
[2] *University of Chinese Academy of Sciences, Beijing 100049, China;*
[3] *Department of Physics, East Carolina University, Greenville, North Carolina 27858, USA;*
[4] *Key Laboratory of Quarks and Lepton Physics (MOE) and Institute of Particle Physics, Central China Normal University, Wuhan 430079, China*

Received May 19, 2018; accepted June 27, 2018; published online August 20, 2018

We study the phase structure of QCD matter in the framework of a multiphase transport model by implementing a strong local parton density fluctuation scenario. Our calculations on the beam energy dependence of net-proton high moment show that local parton density fluctuation only has a small effect. But it becomes important when all baryons are included. We then study the effect on elliptic flow and find that an enhanced local parton density fluctuation leads to a significant effect on protons but a small effect on pions. Our study provides a reference of transport dynamics on QCD phase transition phenomena and will be relevant for the upcoming phase II of the beam energy scan program at RHIC.

QCD phase diagram, parton density fluctuation, AMPT model

PACS number(s): 25.75.Dw, 25.40.Ep, 25.75.Nq

Citation: X. H. Jin, J. H. Chen, Z. W. Lin, G. L. Ma, Y. G. Ma, and S. Zhang, Explore the QCD phase transition phenomena from a multiphase transport model, Sci. China-Phys. Mech. Astron. **62**, 011012 (2019), https://doi.org/10.1007/s11433-018-9272-4

1 Introduction

Lattice QCD is a fundamental tool to study the thermodynamics of QCD matter at small chemical potential, but at large baryon chemical potential it suffers from the sign problem [1-3]. First-principle calculations face the breakdown of perturbative theory at low energy scales. From this point of view, experimental programs provide a unique chance to learn about the QCD thermodynamics that is not yet accessible to theoretical calculations. Indeed, searching for the QCD critical point, phase transition signatures and mapping the QCD phase diagram are major scientific goals of the beam energy scan (BES) program in heavy-ion collisions [4]. Existing data from SPS and phase I of the BES program at RHIC show interesting features of the QCD matter close to the phase transition boundary. They include the beam energy dependence of anisotropic collective flow [5, 6], the sign change of the slope of the proton directed flow [7], the non-monotonic variation of higher moments of the net proton distribution [8-11], the global polarization of Λ hyperons, the charge separation of identified particle along the magnetic field [12,13] and the production of light nuclei [14,15]. These results indicate the rich physics of QCD matter close to the critical point region.

However, there are still large statistical uncertainties on the experimental data, therefore solid conclusions can not be reached at this stage. The plan for phase II of the BES at RHIC is to reduce the statistical uncertainty, and many theoretical studies will be needed. In this paper, we try to explore the QCD phase transition phenomena in a multiphase transport model by implementing a strong local parton density fluctuation in prior to hadronization. We argue that such

*Corresponding authors (JinHui Chen, email: chenjinhui@sinap.ac.cn; YuGang Ma, email: mayugang@sinap.ac.cn)

an effect could be a good representation of QCD phase transition. Event-by-event fluctuations of net-baryon, net-charge and net-strangeness are expected to be sensitive to the QCD critical point [16]. Thus in this paper we will focus on the response of event-by-event fluctuations of net-proton and net-baryon to the enhanced local parton density fluctuation. We then extend our study to the elliptic flow observable. The paper is organized as follows. In sect. 2 we describe the relationship of theoretical calculations and experimental observables. In sect. 3 we briefly introduce the AMPT model and describe in detail how we add enhanced local parton density fluctuations into the AMPT model. Then the beam energy and rapidity window dependence of net-proton and net-baryon number fluctuations are presented, together with the effects on the elliptic flow. Finally a summary is given.

2 Fluctuation of conserved charges

Fluctuations have long been considered as sensitive observables in heavy-ion collisions to explore the phase structure and map the QCD phase diagram [17]. Most fluctuation measures related to quadratic variances of event-by-event observables, such as particle multiplicities, net charge, baryon number and particle ratios. The singular contribution to quadratic variances induced by the proximity of the critical point is proportional to approximately ξ^2, where ξ is the correlation length. For higher moments, such as, the fourth moment grows as ξ^7 near the critical point [18]. In a grand-canonical ensemble, the pressure of the thermal system can be expressed as the logarithm of the QCD partition function:

$$\frac{P}{T^4} = \frac{1}{VT^3}\ln[Z(V,T,\mu_{\rm B},\mu_{\rm Q},\mu_{\rm S})], \tag{1}$$

where V and T are respectively the system volume and temperature, while $\mu_{\rm B}$, $\mu_{\rm Q}$ and $\mu_{\rm S}$ are the chemical potentials of the baryon number, electric charge and strangeness, respectively. The susceptibility of the conserved charges can be expressed as partial derivatives of the pressure with respect to the corresponding chemical potentials [19]:

$$\chi^{\rm BQS}_{ijk} = \frac{\partial^{i+j+k}[P/T^4]}{\partial(\mu_{\rm B}/T)^i\partial(\mu_{\rm Q}/T)^j\partial(\mu_{\rm S}/T)^k}. \tag{2}$$

The cumulants of multiplicity distributions of the baryon number, electric charge and strangeness are connected with the generalized susceptibilities by

$$C^{\rm BQS}_{ijk} = \frac{\partial^{i+j+k}\ln[Z(V,T,\mu_{\rm B},\mu_{\rm Q},\mu_{\rm S})]}{\partial(\mu_{\rm B}/T)^i\partial(\mu_{\rm Q}/T)^j\partial(\mu_{\rm S}/T)^k} = VT^3\chi^{\rm BQS}_{ijk}. \tag{3}$$

In order to cancel the volume dependence, we construct the ratios of cumulants as the observables.

Experimentally, we use $N = N_q - N_{\bar{q}}$ to denote the number of net conserved charge in one event and $\langle N\rangle$ to denote the mean value over all events, where q = B, Q or S. The deviation of N from $\langle N\rangle$ is defined as $\delta N = N - \langle N\rangle$. The cumulants of these conserved charges can be written as:

$$C_{1,N} = \langle N\rangle, \tag{4}$$
$$C_{2,N} = \langle(\delta N)^2\rangle, \tag{5}$$
$$C_{3,N} = \langle(\delta N)^3\rangle, \tag{6}$$
$$C_{4,N} = \langle(\delta N)^4\rangle - 3\langle(\delta N)^2\rangle^2. \tag{7}$$

After various cumulants are constructed, the central moments of the distribution of conserved charges are calculated in the following way:

$$M = C_{1,N}, \tag{8}$$
$$\sigma^2 = C_{2,N}, \tag{9}$$
$$S = \frac{C_{3,N}}{(C_{2,N})^{3/2}}, \tag{10}$$
$$\kappa = \frac{C_{4,N}}{(C_{2,N})^2}. \tag{11}$$

To cancel the volume dependence, the following high-moment ratios are used as the observables [18]:

$$S\sigma = \frac{C_{3,N}}{C_{2,N}}, \tag{12}$$
$$\kappa\sigma^2 = \frac{C_{4,N}}{C_{2,N}}. \tag{13}$$

3 The AMPT model

The AMPT model is a multiphase transport model that has been used extensively to simulate the dynamics evolution of high energy heavy-ion collisions [20]. The string melting version of the AMPT model includes four main components. Hadrons from the fragmentation of excited strings from the heavy ion jet interaction generator (HIJING) model are decomposed into quarks and antiquarks as the initial condition [21]. Then scattering among partons are modeled by Zhang's parton cascade [22], where the cross section is obtained from the perturbative QCD with quark screening masses. Next, a quark coalescence model is used to implement the phase transition from partons to hadrons. At last, the dynamics of the subsequent hadronic matter is described by the extended version of a relativistic transport (ART) model [23].

As discussed above, the correlation length ξ would diverge at the critical point in an idealized thermodynamic limit. In a real system, the magnitude of the ξ is limited by the system size and in heavy ion collision the divergence of ξ is

cut off by the effects of critical slowing down, and the estimates of the maximum correlation length are in the range of at most 2-3 fm, compared to the natural 0.5-1 fm away from the critical point [8]. This larger correlation length may cause a bigger fluctuation in the coordinates and momentum of the fireball. In order to explore the QCD phase transition signals in a wide collision energy range covered by the BES program at RHIC [4], we extend the AMPT model (version v1.26t5/v2.26t5) with an enhanced local parton density fluctuation (ELDF), where exact strangeness and baryon charge conservation are taken into account. Specifically, we assume that the partonic matter just prior to hadronization is made of a number of clusters in the transverse plane. In our implementation, the center position of each cluster is determined by the local maximum of parton density at freeze-out in each event. The cluster number and size are free parameters. In our study, the transverse radius of each cluster is set as 1 fm, and the number of cluster is randomly selected from the values of 2, 3, 4 and 5. To create the clusters, we move each parton outside the cluster regions into a random transverse location inside the closest cluster, while the longitudinal coordinate and the momentum of the parton are not changed [24]. Figure 1 shows the transverse coordinate space distribution of hadrons right after coalescence without (Figure 1(a)) and with (Figure 1(b)-(e)) parton cluster formations.

We can see that the parton fluctuation effect is retained in the initial hadrons right after hadronization in this extended AMPT model. Although each event has a specific number of clusters, a large event sample consists of events with different numbers of clusters and may represent a chaotic distribution. We then calculate the baryon number fluctuations in Au+Au collisions at $\sqrt{s_{NN}}$ = 7.7, 11.5 and 19.6 GeV in this version (denoted as ELDF AMPT). The original AMPT model calculations are also performed for comparison. For our study, we chose the 0-5% centrality with event statistics of 10^6 at each energy.

4 Transverse momentum spectra and rapidity distributions

Figure 2 shows the π^+ and proton p_T spectra in central Au+Au collisions at $\sqrt{s_{NN}}$ = 7.7, 11.5 and 19.6 GeV. We see that AMPT describes the midrapidity π^+ and proton data well. Differences between the original AMPT model and the ELDF AMPT model are very small. One can further confirm that the difference is small since the two smooth dashed lines in each panel of Figure 2 almost fully overlap. This is related to the fact that the ELDF AMPT model only changes the transverse coordinate space distribution of partons while it keeps the parton momenta and total parton number in the event unchanged. The same features can be seen in the rapidity distributions of π^+ and protons, as shown in Figure 3, where the rapidity distribution of π^+ and proton in

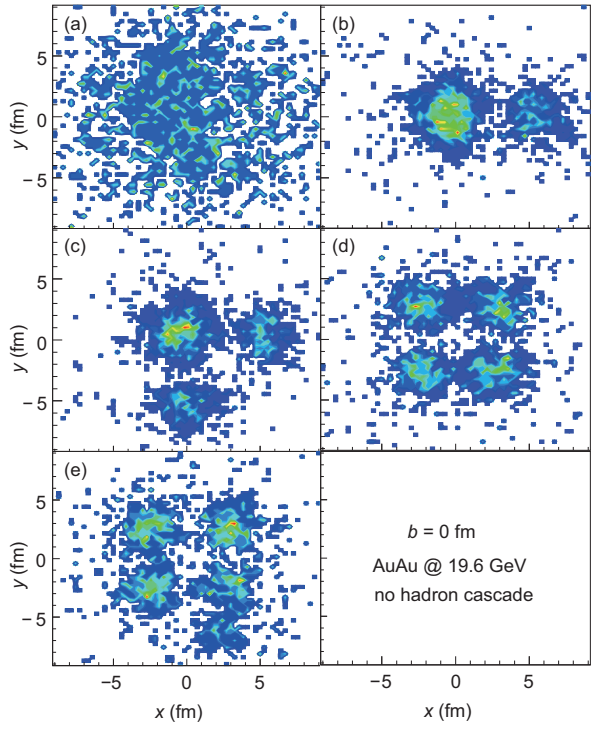

Figure 1 (Color online) Initial spatial distribution of hadrons in a central Au+Au collision at $\sqrt{s_{NN}}$ = 19.6 GeV in the AMPT model just after hadronization. (a) The original AMPT model. (b), (c), (d) and (e) are from the ELDF AMPT model with cluster number of 2, 3, 4 and 5, respectively, for the same event.

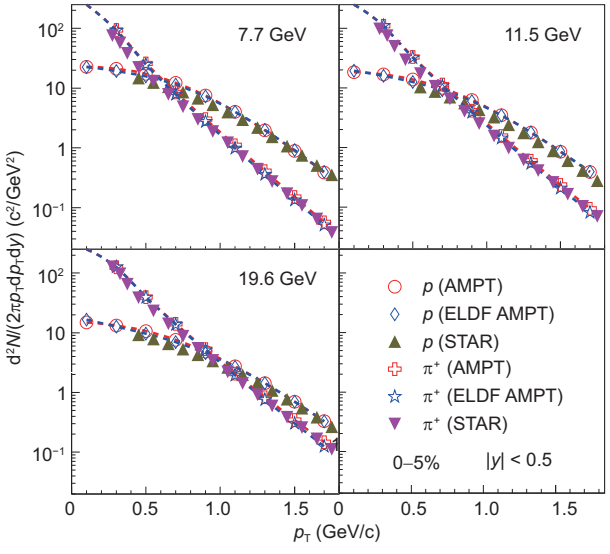

Figure 2 (Color online) Transverse momentum spectra of π^+ and proton in Au+Au collisions at $\sqrt{s_{NN}}$ = 7.7, 11.5 and 19.6 GeV. Open symbols represent model results, and fill symbols are experimental data from STAR Collaboration [25]. Dashed curves are smooth lines for the open symbols.

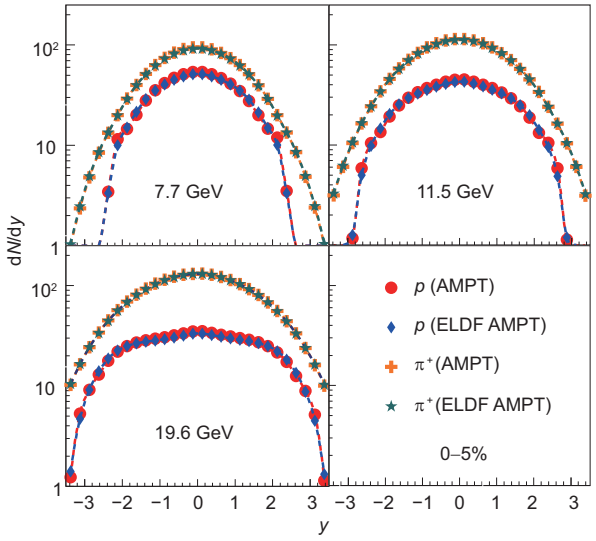

Figure 3 (Color online) Rapidity distributions of π^+ and proton in central Au+Au collisions at $\sqrt{s_{NN}}$ = 7.7, 11.5 and 19.6 GeV from AMPT and ELDF AMPT.

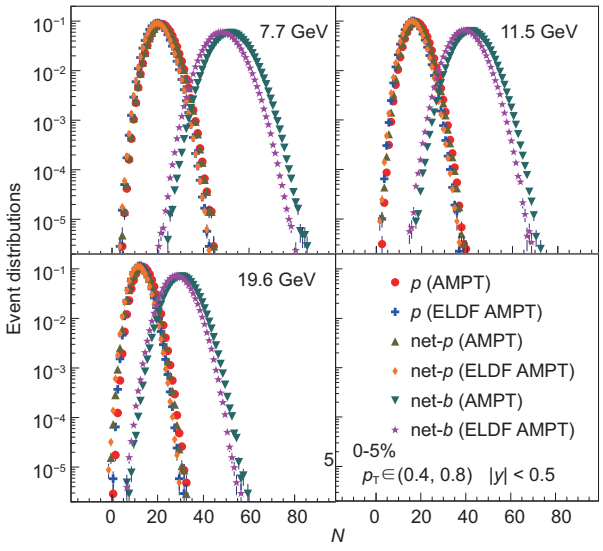

Figure 4 (Color online) Event-by-event proton, net-proton and net-baryon multiplicity distributions in central Au+Au collisions at $\sqrt{s_{NN}}$ = 7.7, 11.5 and 19.6 GeV from the original AMPT model and the ELDF AMPT model.

the original AMPT model and the ELDF AMPT model are close to each other.

5 Results and discussion

For the calculations of net baryon number fluctuation, we apply the same kinematic cuts and analysis method as used in experiment data [11]. And the statistical error is estimated by the Delta theorem [26]. Event-by-event proton, net-proton and net-baryon multiplicity distributions for various collisions energy measured within $0.4 < p_{\rm T} < 0.8$ GeV/c and $|y| < 0.5$ are shown in Figure 4. The shapes of proton, net-proton and net-baryon distributions from AMPT are almost the same as those in ELDF AMPT, while the mean values of the distributions are a bit lower in ELDF AMPT. It is because ELDF affects the phase space distribution of hadrons from quark coalescence.

In Figure 5 we show the energy dependence of $\kappa\sigma^2$ of proton, net-proton, net-nucleon and net-baryon from the original AMPT and ELDF AMPT in comparison with the STAR experimental data. For the proton and net-proton results, our calculations show a slight energy dependence, consistent with early studies by other groups using the original AMPT model [27, 28]. Although our study includes contributions from the local parton density fluctuation, the difference from the original AMPT model calculations is small, as shown in the up panel of Figure 5. When neutrons and all other baryons are also taken into account, as shown in the down panel of Figure 5, we see that the effects of these other baryons on $\kappa\sigma^2$ can be significant, especially at lower energies.

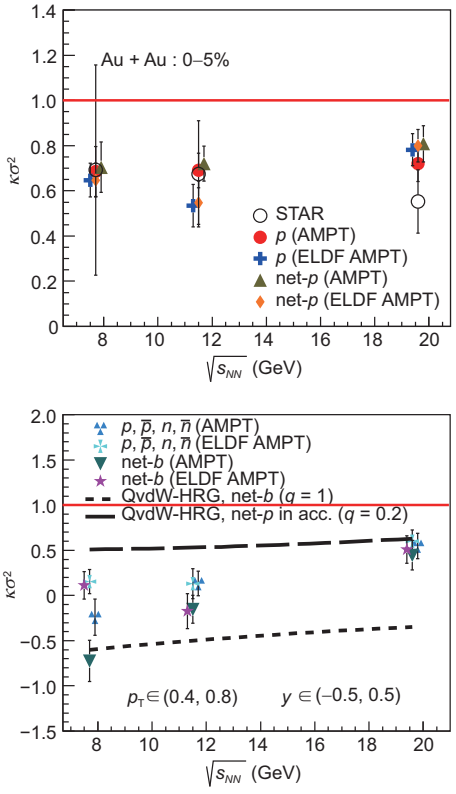

Figure 5 (Color online) The energy dependence of high-moment ratio ($\kappa\sigma^2$) of proton, net-proton, net-nucleon and net-baryon in central Au + Au collisions at $\sqrt{s_{NN}}$ = 7.7, 11.5 and 19.6 GeV from the original AMPT and ELDF AMPT model. The results have been shifted slightly in $\sqrt{s_{NN}}$ for clarity. In the up panel, the experimental data [11] are added for comparison. In the down panel, results of net baryon number fluctuations in different acceptance windows from the QvdW-HRG [19] model are included for comparison.

We further investigate this difference by turning off the hadronic interaction stage in the AMPT model, as shown in Figure 6. Comparing the up panel of Figures 5 and 6, we see that hadronic interactions have a large effect on the net-proton high moment at $\sqrt{s_{NN}}$ = 7.7 GeV but small effects at $\sqrt{s_{NN}}$ = 11.5 and 19.6 GeV. A similar feature is found for net-baryon, where the hadron cascade has an important effect, especially at lower collision energies. Our results are in agreement with other models, for example, the QvdW-HRG model [19], which calculations with different acceptance windows are shown in Figures 5 and 6.

The acceptance dependence of fluctuations is another important question. We study the high-moment ratios of proton, net-proton, nucleon and net-baryon distributions as a function of the rapidity window in Figure 7. The results from AMPT and ELDF AMPT both show a clear dependence on the rapidity window selection, similar to other calculations [29, 30]. A larger rapidity window always leads to a larger fluctuation signal.

The local parton density fluctuation that we introduce may affect other observables such as elliptic flow. It is naive to expect that parton density fluctuation can be reflected in the final particle momentum space via quark coalescence and hadron interactions. Thus a detail study on elliptic flow will be interesting. In the following, we evaluate the effect of local parton density spatial distributions on elliptic flow. Elliptic

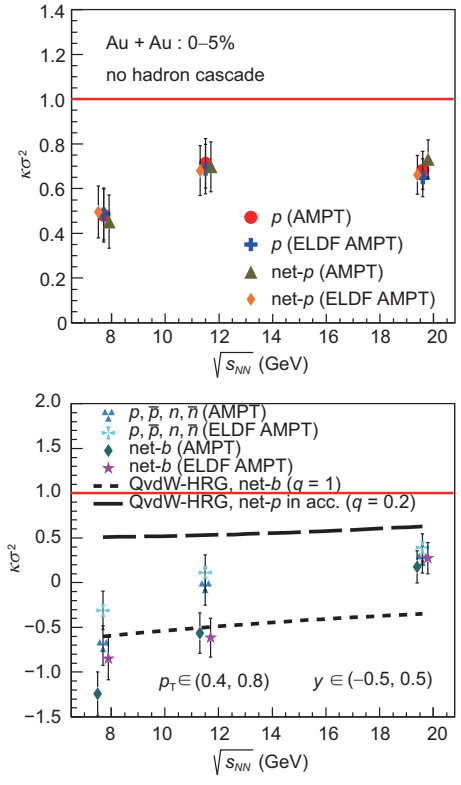

Figure 6 (Color online) Similar to Figure 5, but for the AMPT model with hadronic transport stage turning off.

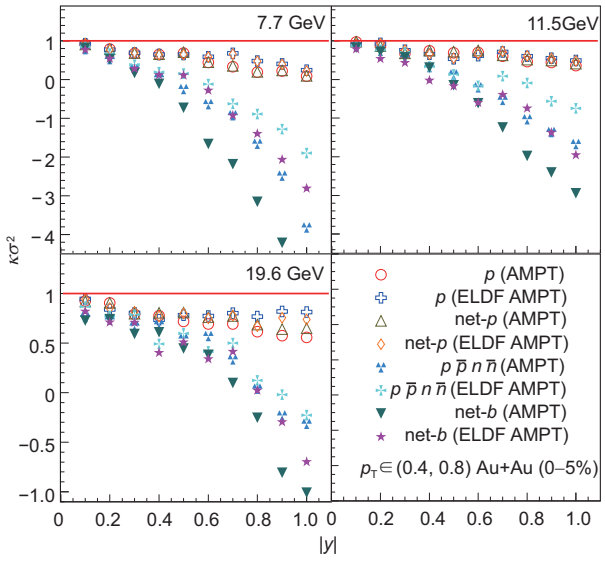

Figure 7 (Color online) Rapidity window dependence of the higher moment ratios of proton, net-proton, nucleon and net-baryon multiplicity distributions in central Au + Au collisions at $\sqrt{s_{NN}}$ = 7.7, 11.5 and 19.6 GeV, where $|y|$ means $|y|_{\max}$, where a bigger $|y|$ represents a bigger y coverage for the analysis.

flow in heavy ion collisions is a measurement of the asymmetry of particle momentum distributions in the transverse plane [31]. The collectivity in high-energy heavy-ion collisions can be measured through the final particle azimuthal anisotropy [32, 33]. The anisotropy coefficients are generally obtained from a Fourier expansion of the final particle azimuthal distribution [34]:

$$E\frac{\mathrm{d}^3N}{\mathrm{d}^3p} = \frac{1}{2\pi}\frac{\mathrm{d}^2N}{p_{\mathrm{T}}\mathrm{d}p_{\mathrm{T}}\mathrm{d}y}\left(1+\sum_{i=1}^{N}2v_n\cos[n(\varphi-\psi_{RP})]\right), \quad (14)$$

where E, p_{T}, y, and φ represent the energy, transverse momentum, rapidity, and azimuthal angle of the particle, respectively; while ψ_{RP} is the reaction plane angle. The Fourier coefficients $v_n(n = 1, 2, 3...)$ are used to characterize the different orders of azimuthal anisotropies with the form

$$v_n = \langle\cos(n[\varphi-\psi_{RP}])\rangle, \quad (15)$$

where the bracket $\langle\rangle$ denotes the averaging over particles and events. In the AMPT model, we calculate the reaction plane angle ψ_{RP} event-by-event using the initial wounded nucleon spatial information.

We now show the elliptic flows of π and proton in the two AMPT models without (Figure 8) or with (Figure 9) hadronic interactions. We see that ELDF AMPT reduces the magnitude of elliptic flow of π and proton in comparison with the original AMPT model. This effect is stronger at higher collisions energies. This is partly because parton clustering moves final partons in the transverse plane and thus artificially destroys much of the collective flow of the final partonic matter. As a result, the coalescence partners ($q\bar{q}$, $3q$, or $3\bar{q}$) tend to

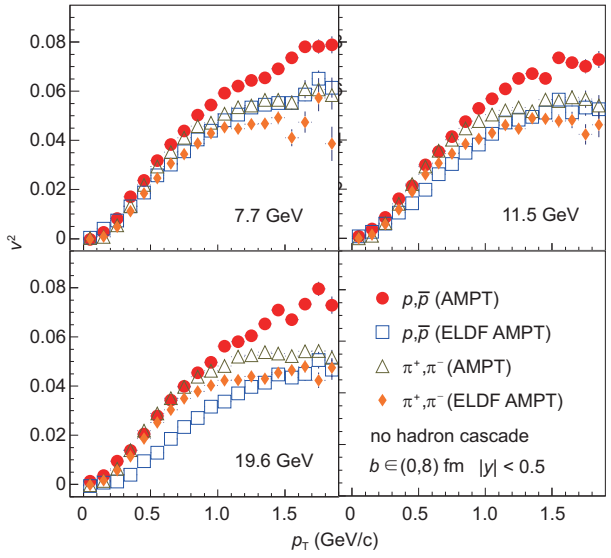

Figure 8 (Color online) The p_T dependence of elliptic flows of π and proton from AMPT just after quark coalescence in Au + Au collisions at $\sqrt{s_{NN}}$ = 7.7, 11.5 and 19.6 GeV.

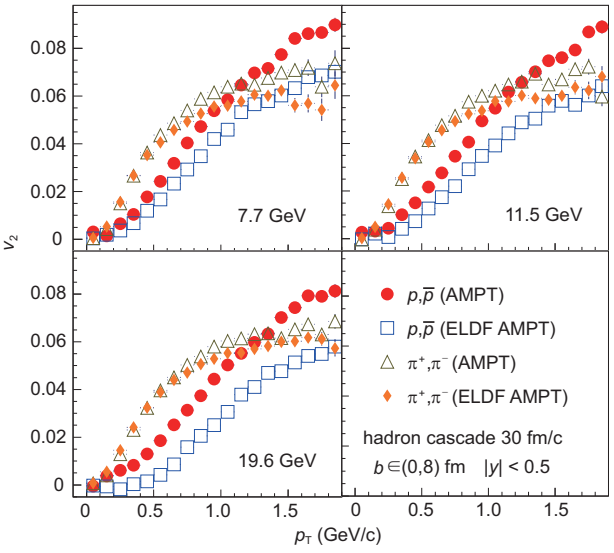

Figure 9 (Color online) Similar to Figure 8, but for hadrons after a 30 fm/c hadron scattering period, which is the typical value used AMPT [20].

have a large opening angle among themselves, which typically leads to a smaller elliptic flow right after coalescence [35]. We note from Figure 9 that hadronic interactions seem to increase the π flow here. Also, the mass splitting of hadron elliptic flows is more clear in Figure 9 after hadron interactions have taken place; consistent with earlier findings [35]. In the ELDF AMPT results, which include a strong local parton density fluctuation, the splitting of elliptic flows between π and proton seems even stronger in Figure 9. This may be due to the fact that clustering tend to increase the initial hadron density and thus increase hadron scatterings, which then cause a bigger v_2 splitting in the ELDF AMPT model.

We note that the current string melting AMPT model used here has some limitations that may affect our results. First, the current quark coalescence model forces the numbers of mesons, baryons, and antibaryons in an event to be separately conserved through quark coalescence process, where only the net-baryon number needs to be conserved [36]. Also, the current string melting AMPT model does not take into account the finite thickness of the incoming nuclei, which would affect the initial parton spatial distribution and density evolution [37]. Note that the effect of finite thickness is especially relevant for the low energies of the beam energy scan program, and there are recent work to improve the AMPT model along these directions [36,37]. In addition, the hadronic mean-field potentials may become important moving to lower collision energies [38], which shall be considered in future development.

6 Summary

In summary, a strong local parton density fluctuation has been implemented in the AMPT model to study its effect on baryon number fluctuations and elliptic flow. We find that the effect on the high moment of net-proton is small. After taking other baryons into account, the high moment of net-baryon from AMPT is significantly different from that of net-proton at lower collision energies, suggesting that hadronic interactions may play an important role in the high moment observables. We also study the rapidity window dependence of net-proton and net-baryon high moments, and find that an appropriate rapidity window shall be carefully chosen when comparing to the experiment data. In addition, we find that the effect of local parton density fluctuation on elliptic flow is small for pions but large for protons, especially at higher collisions energies. Our study provides valuable information on exploring the QCD phase diagram, for example, at the beam energy scan program at RHIC [4].

This work was supported by the Major State Basic Research Development Program in China (Grant Nos. 2014CB845400, and 2015CB856904), and the National Natural Science Foundation of China (Grant Nos. 11775288, 11421505, 11628508, and 11520101004). We are grateful to insight discussion with Prof. HuanZhong Huang.

1 O. Kaczmarek, and F. Zantow, Phys. Rev. D **71**, 114510 (2005).
2 M. Cheng, N. H. Christ, S. Datta, J. van der Heide, C. Jung, F. Karsch, O. Kaczmarek, E. Laermann, R. D. Mawhinney, C. Miao, P. Petreczky, K. Petrov, C. Schmidt, and T. Umeda, Phys. Rev. D **74**, 054507 (2006).
3 R. Gupta, arXiv: hep-lat/9807028.
4 M. M. Aggarwal, et al. (STAR Collaboration), arXiv: 1007.2613.

5 D. Teaney, J. Lauret, and E. V. Shuryak, Phys. Rev. Lett. **86**, 4783 (2001).
6 L. Adamczyk, et al. (STAR Collaboration), Phys. Rev. Lett. **110**, 142301 (2013), arXiv: 1301.2347.
7 L. Adamczyk, et al. (STAR Collaboration), Phys. Rev. Lett. **112**, 162301 (2014), arXiv: 1401.3043.
8 M. Nahrgang, T. Schuster, M. Mitrovski, R. Stock, and M. Bleicher, Eur. Phys. J. C **72**, 2143 (2012), arXiv: 0903.2911.
9 A. Bzdak, V. Koch, and V. Skokov, Phys. Rev. C **87**, 014901 (2013), arXiv: 1203.4529.
10 M. M. Aggarwal, et al. (STAR Collaboration), Phys. Rev. Lett. **105**, 022302 (2010), arXiv: 1004.4959.
11 L. Adamczyk, et al. (STAR Collaboration), Phys. Rev. Lett. **112**, 032302 (2014).
12 L. Adamczyk, et al. (STAR Collaboration), Nature **548**, 62 (2017), arXiv: 1701.06657.
13 L. Adamczyk, et al. (STAR Collaboration), Phys. Rev. Lett. **113**, 052302 (2014).
14 K. J. Sun, L. W. Chen, C. M. Ko, and Z. B. Xu, Phys. Lett. B **774**, 103 (2017), arXiv: 1702.07620.
15 K. J. Sun, L. W. Chen, C. M. Ko, J. Pu, and Z. B. Xu, Phys. Lett. B **781**, 499 (2018), arXiv: 1801.09382.
16 H. Petersen, Nucl. Phys. A **967**, 145 (2017), arXiv: 1704.02904.
17 X. F. Luo, and N. Xu, Nucl. Sci. Tech. **28**, 112 (2017).
18 C. Zhou, J. Xu, X. F. Luo, and F. Liu, Phys. Rev. C **96**, 014909 (2017), arXiv: 1703.09114.
19 V. Vovchenko, L. J. Jiang, M. I. Gorenstein, and H. Stoecher, arXiv: 1711.07260.
20 Z. W. Lin, S. Pal, C. M. Ko, B. A. Li, and B. Zhang, Phys. Rev. C **64**, 011902 (2001).
21 X. N. Wang, and M. Gyulassy, Phys. Rev. D **44**, 3501 (1991).
22 B. Zhang, Comput. Phys. Commun. **109**, 193 (1998).
23 B. A. Li, and C. M. Ko, Phys. Rev. C **52**, 2037 (1995).
24 X. H. Jin, J. H. Chen, Y. G. Ma, S. Zhang, C. J. Zhang, and C. Zhong, Nucl. Sci. Tech. **29**, 54 (2018).
25 L. Adamczyk, et al. (STAR Collaboration), Phys. Rev. C **96**, 044904 (2017).
26 X. F. Luo, Phys. Rev. C **91**, 034907 (2015), arXiv: 1410.3914.
27 Y. F. Lin, L. Z. Chen, and Z. M. Li, Phys. Rev. C **96**, 044906 (2017), arXiv: 1707.04375.
28 Y. Zhou, S. S. Shi, K. Xiao, K. J. Wu, and F. Liu, Phys. Rev. C **82**, 014905 (2010), arXiv: 1004.2558.
29 A. Bzdak, and V. Koch, Phys. Rev. C **86**, 044904 (2012), arXiv: 1206.4286.
30 B. Ling, and M. A. Stephanov, Phys. Rev. C **93**, 034915 (2016), arXiv: 1512.09125.
31 J. Y. Ollitrault, Nucl. Phys. A **638**, 195c (1998).
32 U. Heinz, and R. Snellings, Annu. Rev. Nucl. Part. Sci. **63**, 123 (2013), arXiv: 1301.2826.
33 H. C. Song, Y. Zhou, and K. Gajdošová, Nucl. Sci. Tech. **28**, 99 (2017).
34 L. Ma, G. L. Ma, and Y. G. Ma, Phys. Rev. C **89**, 044907 (2014), arXiv: 1404.5935.
35 H. L. Li, L. He, Z. W. Lin, D. Molnar, F. Q. Wang, and W. Xie, Phys. Rev. C **93**, 051901 (2016), arXiv: 1601.05390; H. L. Li, L. He, Z. W. Lin, D. Molnar, F. Q. Wang, and W. Xie, Phys. Rev. C **96**, 014901 (2017), arXiv: 1604.07387.
36 Y. C. He, and Z. W. Lin, Phys. Rev. C **96**, 014910 (2017), arXiv: 1703.02673.
37 Z. W. Lin, arXiv: 1704.08418.
38 C. J. Zhang, and J. Xu, Phys. Rev. C **96**, 044907 (2017), arXiv: 1707.07272.